Teardrop and parabolic lens yield curves for viscous-plastic sea ice models: New constitutive equations and failure angles

Damien Ringeisen[1], Martin Losch[2], and Bruno Tremblay[1]

[1]McGill University
[2]Alfred Wegener Institute for Polar and Marine Research

December 7, 2022

Abstract

Most viscous-plastic sea ice models use the elliptical yield curve. This yield curve has a fundamental flaw: it excludes acute angles between deformation features at high resolution. Conceptually, the teardrop and parabolic lens yield curves offer an attractive alternative. These yield curves feature a non-symmetrical shape, a Coulombic behavior for the low-medium compressive stress, and a continuous transition to the ridging-dominant mode. We show that the current formulation of the teardrop and parabolic lens viscous-plastic yield curves with normal flow rules results in negative or zero bulk and shear viscosities and, consequently, poor numerical convergence and representation of stress states on or within the yield curve. These issues are mainly linked to the assumption that the constitutive equation applicable to the elliptical yield curve also applies to non-symmetrical yield curves and yield curves with tensile strength. We present a new constitutive relation for the teardrop and parabolic lens yield curves that solves the numerical convergence issues naturally. Results from simple uni-axial loading experiments show that we can reduce the residual norm of the numerical solver with a smaller number of total solver iterations, resulting in significant improvements in numerical efficiency and representation of the stress and deformation field. These yield curves lead to smaller angles of failure, in agreement with theoretical predictions, and are good candidates to replace the elliptical yield curve in high-resolution pan-arctic sea ice simulation.

1

1 # Teardrop and parabolic lens yield curves for
2 # viscous-plastic sea ice models: New constitutive
3 # equations and failure angles

4 **Damien Ringeisen[1,2,3], Martin Losch[1], L.Bruno Tremblay[3]**

5 [1]Alfred-Wegener-Institut, Helmholtz-Zentrum für Polar- und Meeresforschung, Bremerhaven, Germany
6 [2]MARUM – Center for Marine Environmental Sciences, Leobener Str. 8, 28359, Bremen, Germany
7 [3]Department of Atmospheric and Oceanic Sciences, McGill University, Montreal, QC, Canada

8 **Key Points:**

9 - Using the constitutive equation of the elliptical yield curve does not always ap-
10 ply to yield curves with other shapes, such as the teardrop.
11 - We propose new constitutive equations for the TD and PL yield curves that solve
12 this problem and improve numerical convergence.
13 - The TD and PL yield curves lead to small failure angles, thus they are candidates
14 to solve the overestimation of the failure angles.

Corresponding author: Damien Ringeisen, `damien.ringeisen@mcgill.ca`

Abstract

Most viscous-plastic sea ice models use the elliptical yield curve. This yield curve has a fundamental flaw: it excludes acute angles between deformation features at high resolution. Conceptually, the teardrop and parabolic lens yield curves offer an attractive alternative. These yield curves feature a non-symmetrical shape, a Coulombic behavior for the low-medium compressive stress, and a continuous transition to the ridging-dominant mode. We show that the current formulation of the teardrop and parabolic lens viscous-plastic yield curves with normal flow rules results in negative or zero bulk and shear viscosities and, consequently, poor numerical convergence and representation of stress states on or within the yield curve. These issues are mainly linked to the assumption that the constitutive equation applicable to the elliptical yield curve also applies to non-symmetrical yield curves and yield curves with tensile strength. We present a new constitutive relation for the teardrop and parabolic lens yield curves that solves the numerical convergence issues naturally. Results from simple uni-axial loading experiments show that we can reduce the residual norm of the numerical solver with a smaller number of total solver iterations, resulting in significant improvements in numerical efficiency and representation of the stress and deformation field. These yield curves lead to smaller angles of failure, in agreement with theoretical predictions, and are good candidates to replace the elliptical yield curve in high-resolution pan-arctic sea ice simulation.

Plain Language Summary

Most sea ice models simulate sea ice as a viscous-plastic material. The stress parametrization in viscous-plastic models commonly uses an elliptical yield curve that delimits between the fast plastic deformations and the slow viscous creep. To overcome some shortcomings of the elliptical yield curve, other shapes of yield curves can be used, like the teardrop and parabolic lens yield curves. In this work, we analyze the current formulation of these two yield curves and show that three problems in these formulations lead to bad numerical convergences and nonphysical behaviors. We propose solutions to each of these problems, and we use a simple experiment to show that our proposed formulation leads to significant improvements in the computing time and the representation of stresses and deformation. We show that these yield curves can create small angles of failure that are not possible with the elliptical yield curve.

1 Introduction

Sea ice dynamical models are an integral part of the CMIP6 models (Notz & Community, 2020). Following the increase of computation power, the models' resolution was increased and can now represent Linear Kinematic Features or LKFs in the sea ice deformation (Hutter et al., 2019; Hutchings et al., 2005). LKFs are narrow bands where most sea ice deformation takes place (Kwok, 2001). Many of the LKFs are leads with open water or thin ice where the bulk of the heat and matter transfer between atmosphere and ocean takes place (Maykut, 1978), so it is important to represent LKFs adequately in sea ice models. The capacity of a sea ice dynamical model to represent LKFs explicitly depends mainly on its resolution and its rheological model (Bouchat et al., 2022; Hutter et al., 2022).

Sea ice deformation is simulated using a rheological model that parameterizes sea ice physical properties and relates stresses and strain rates. Multiple sea-ice rheological models have been proposed:: Elastic-Plastic (EP, Coon et al., 1974), Viscous-Plastic (VP, Hibler, 1977), Elastic-Anisotropic-Plastic (EAP, Tsamados et al., 2013), or Maxwell-Elasto-Brittle (MEB, Dansereau et al., 2016). Still today, sea ice models most commonly use the VP rheological model because in spite of critique (Girard et al., 2009), they perform well compared to observations and other rheologies, especially at high resolution (Hutter et al., 2022).

The VP rheological model requires the definition of a yield curve and a flow rule. First, the yield curve sets the stress limit at which sea ice deforms plastically. Several yield curve shapes have been used: elliptical (Hibler, 1979), the sine-wave lens (Bratchie, 1984), triangular or Mohr–Coulomb (Ip et al., 1991; Hibler & Schulson, 2000; Tremblay & Mysak, 1997), and teardrop or parabolic lens (Zhang & Rothrock, 2005). Second, the flow rule sets the relative amount of shear and divergence or convergence of the ice for a given stress state. The flow rule can be normal (Hibler, 1979; Zhang & Rothrock, 2005) or non-normal (Ip et al., 1991; Ringeisen et al., 2021) to the yield curve. In this terminology, a rheology is defined by a specific yield curve shape and a flow rule.

Rothrock (1975) proposed two yield curve shapes: the teardrop and parabolic lens yield curves. These two yield curves satisfy Drucker's convexity postulate for stability (Palmer et al., 1967; Drucker, 1950), as the elliptical yield curve. The Mohr–Coulomb yield curve, however, does not satisfy a strict convexity criterion, as it has straight parts.

79   The TD and PL yield curves also represent both divergence and convergence, in contrast

80   to a Mohr–Coulomb yield curve with a normal flow rule. These two yield curve shapes

81   have not been used until Zhang and Rothrock (2005) proposed VP constitutive equa-

82   tions of these yield curves with normal flow rules. These sea ice VP rheologies are im-

83   plemented in the PIOMAS model (Zhang, 2020) but, to our knowledge, have not been

84   used much elsewhere.

85   All sea ice models create too many large intersection angles (Hutter et al., 2022):

86   Large intersection angles prevail in sea ice models, whereas small intersection angles pre-

87   vail in observations. This discrepancy is present in the standard VP rheology as well as

88   more recent rheological models like the MEB or the EAP. However, results from Hutter

89   et al. (2022) also show that changing the size of the elliptical yield curve can lead to bet-

90   ter results, following the results of Bouchat and Tremblay (2017). Experiments with el-

91   liptical curves show that, within the sea ice VP rheology, the intersection angles can be

92   linked to the shape of the yield curve (Ringeisen et al., 2019) and the orientation of the

93   flow rule (Ringeisen et al., 2021). Stress measurement of sea ice failure stresses show that

94   the yield envelope agrees well with the Mohr–Coulomb or the Teardrop yield curve shape

95   (Schulson, 2004; Richter-Menge & Jones, 1993; Iliescu & Schulson, 2004), in agreement

96   with the observation of a preferred small angle of fracture (Erlingsson, 1988). Yet, these

97   non-elliptical yield curves have yet to be implemented and investigated for the creation

98   of angles.

99   Sea ice models require expensive solvers because of the non-linear equations of the

100 rheology (Lemieux & Tremblay, 2009; Losch & Danilov, 2012; Koldunov et al., 2019).

101 For useful climate modeling, sea ice models need to be stable and efficient while giving

102 an accurate prediction of sea ice motion. The stability of the sea ice model can be ex-

103 pressed by system energy considerations (Dukowicz, 1997; Schulkes, 1996; Pritchard, 2005).

104 For example, a negative bulk viscosity would make the rheology act as a spurious en-

105 ergy source that leads to model instabilities. Instabilities lead to poor numerical con-

106 vergence and inefficiency as the numerical convergence is more difficult to obtain.

107 In this paper, we document three issues in the formulation of the Teardrop (TD)

108 and Parabolic Lens (PL) yield curves with normal flow rules, as they are described in

109 Zhang and Rothrock (2005). First and second, regions of the yield curve where the non-

110 linear viscosity coefficients are negative or zero and become sources of energy instead of

sinks, and third, an inconsistency in the capping of the viscosities for the viscous regime

prevents the stresses from remaining on or within the yield curve. We then propose so-

lutions to these issues that improve numerical convergence for high-resolution sea ice mod-

els. We test these solutions in an idealized experiment and show that they lead to im-

proved numerical convergence and efficiency. Finally, we explore the angles of failure ob-

tained with these two rheologies and show that they are good candidates to replace the

elliptical yield curve.

The paper is structured as follows: Section 2 reviews the original TD and PL viscous-

plastic rheologies (Zhang & Rothrock, 2005). Section 3 discusses the problems and so-

lutions in detail. Section 4 describes an idealized experiment used to compare the new

and original rheology. Section 5 compares the numerical convergence between the orig-

inal and new formulations and investigates the failure angles created with the TD and

PL yield curves. The discussion is presented in Sect. 6, followed by the Summary and

conclusions in Sect. 7.

2 Sea ice model

2.1 The sea ice viscous-plastic rheological model

Following general practice, we simulate sea ice as a (vertically integrated) 2D viscous-

plastic material. The ice velocities are calculated from the sea ice momentum equations:

$$\rho\, h \frac{\partial \mathbf{u}}{\partial t} = -\rho\, h\, f\, \mathbf{k} \times \mathbf{u} + \tau_{\mathbf{a}} + \tau_{\mathbf{o}} - \rho\, h\, \nabla \Phi_s + \nabla \cdot \boldsymbol{\sigma}, \tag{1}$$

where ρ is the ice density, h is the mean sea ice thickness, $\mathbf{u}$ is the ice drift velocity field,

f is the Coriolis parameter, $\mathbf{k}$ is the vertical unit, $\tau_{\mathbf{a}}$ is the surface air stress, $\tau_{\mathbf{o}}$ is the

ocean drag, $\nabla \Phi_s$ is the acceleration due to the gradient of geopotential (i.e., sea surface)

height, and $\boldsymbol{\sigma}$ is the vertically integrated internal ice stress tensor defined by the sea ice

VP constitutive equations.

We use the constitutive equation for the elliptical yield curve (Hibler, 1979, 1977):

$$\sigma_{ij} = 2\eta\dot{\epsilon}_{ij} + (\zeta - \eta)\, \dot{\epsilon}_{kk}\delta_{ij} - \frac{P}{2}\delta_{ij}, \tag{2}$$

where ζ and η are the bulk and shear viscosities, and $\dot{\epsilon}_{ij}$ are the strain rates defined as

$\dot{\epsilon}_{ij} = \frac{1}{2}\left(\frac{\partial u_i}{\partial x_j} + \frac{\partial u_j}{\partial x_i}\right)$. Different VP rheologies have different non-linear relationships be-

tween the viscosities and the strain rates.

The local isotropic ice compressive strength P is defined as a function of the mean ice thickness h and concentration A, as

$$P = P^{\star}\, h\, e^{-C^{\star}(1-A)},\tag{3}$$

where $P^{\star}$ is the compressive strength of $1\,\mathrm{m}$ thick ice and $C^{\star}$ is a model parameter defining the ice strength dependence on ice concentration.

Equation (2) can also be written in stress invariant form as

$$\sigma_{\mathrm{I}} = 2\zeta\dot{\epsilon}_{\mathrm{I}} - \frac{P}{2},\tag{4}$$

$$\sigma_{\mathrm{II}} = 2\eta\dot{\epsilon}_{\mathrm{II}},\tag{5}$$

where the stress invariants are

$$\sigma_{\mathrm{I}} = \frac{1}{2}\left(\sigma_{11} + \sigma_{22}\right) \text{ and } \sigma_{\mathrm{II}} = \frac{1}{2}\sqrt{(\sigma_{11} - \sigma_{22})^2 + 4\sigma_{12}^2},\tag{6}$$

and the strain rate invariants are

$$\dot{\epsilon}_{\mathrm{I}} = \frac{1}{2}\left(\dot{\epsilon}_{11} + \dot{\epsilon}_{22}\right) \text{ and } \dot{\epsilon}_{\mathrm{II}} = \frac{1}{2}\sqrt{(\dot{\epsilon}_{11} - \dot{\epsilon}_{22})^2 + 4\dot{\epsilon}_{12}^2}.\tag{7}$$

With the factor $\frac{1}{2}$ for $\dot{\epsilon}_{\mathrm{I}}$ and $\dot{\epsilon}_{\mathrm{II}}$, we follow the definition of the strain rate invariants given in Zhang and Rothrock (2005).

2.2 Original formulations

Following Zhang and Rothrock (2005), the equation of the teardrop (TD) and the parabolic lens (PL) yield curves can be written as

$$\frac{\sigma_{\mathrm{II}}}{P} = -\left(\frac{\sigma_{\mathrm{I}}}{P} - k_t\right)\left(1 + \frac{\sigma_{\mathrm{I}}}{P}\right)^q,\tag{8}$$

where $q = \frac{1}{2}$ for the TD and $q = 1$ for the PL yield curve. P is the local isotropic ice compressive strength (Eq. 3) and $k_t = T/P$ is the tensile factor such that T is the local isotropic ice tensile strength (König Beatty & Holland, 2010). Note that the original formulation used a instead of k_t, we changed the notation to be more consistent with more recent literature. Equation (8) can be rewritten as

$$F = y + (x - k_t)(1 + x)^{\frac{1}{2}} = 0, \text{ for the TD},\tag{9}$$

$$F = y + (x - k_t)(1 + x) = 0, \text{ for the PL},\tag{10}$$

where

$$x = \frac{\sigma_{\mathrm{I}}}{P}\ ,\ y = \frac{\sigma_{\mathrm{II}}}{P}.\tag{11}$$
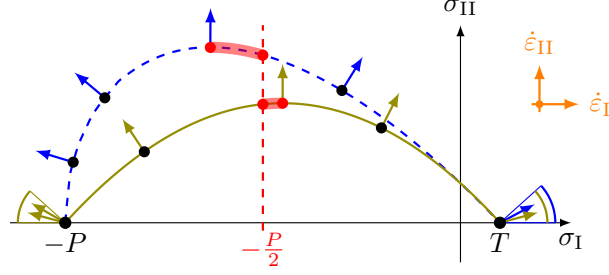
Figure 1. Representation of the teardrop and parabolic yield curves with a normal flow rule in invariant stress space (σ_I, σ_{II}) with $k_t = 0.1$. Regions of the yield curve where bulk viscosities are negative are shown as a thick red (see Sec. 3.1). The angles at the tips show the range of flow rule grouped at this point.

Equations (9) or (10), together with the associated flow rule conditions,

$$\dot{\epsilon}_I = \lambda \frac{\partial F}{\partial x} \frac{\partial x}{\partial \sigma_I} = \frac{\lambda}{P} \frac{\partial F}{\partial x}, \quad \dot{\epsilon}_{II} = \lambda \frac{\partial F}{\partial y} \frac{\partial y}{\partial \sigma_{II}} = \frac{\lambda}{P} \frac{\partial F}{\partial x}, \tag{12}$$

constitute systems of three equations and three unknowns $(\sigma_I, \sigma_{II}, \lambda)$ or (x, y, λ). The solution of these systems can be written as

$$\left. \begin{array}{ll} x_{\text{TD}} = \dfrac{\sigma_I}{P} = \dfrac{-[6 - 3k_t - 2l^2] + 2l\sqrt{l^2 + 3(1 + k_t)}}{9}, & \text{(13)} \\[3mm] y_{\text{TD}} = \dfrac{\sigma_{II}}{P} = -(x_{\text{TD}} - k_t)(1 + x_{\text{TD}})^{\frac{1}{2}}, & \text{(14)} \\[3mm] \lambda = P\dot{\epsilon}_{II}, & \text{(15)} \end{array} \right\} \text{ for the TD,}$$

and

$$\left. \begin{array}{ll} x_{\text{PL}} = \dfrac{\sigma_I}{P} = \dfrac{1}{2}(l - 1 + k_t), & \text{(16)} \\[3mm] y_{\text{PL}} = \dfrac{\sigma_{II}}{P} = -(x_{\text{PL}} - k_t)(1 + x_{\text{PL}}), & \text{(17)} \\[3mm] \lambda = P\dot{\epsilon}_{II}, & \text{(18)} \end{array} \right\} \text{ for the PL,}$$

where $l = \frac{\dot{\epsilon}_I}{\dot{\epsilon}_{II}}$. Note that a second root for x_{TD} is discarded because it leads to flow rules pointing inward of the yield curve (not shown). The bulk and shear viscosities ζ and η can be calculated from the above constitutive equations (Eqs. 4-5) as,

$$\left. \begin{array}{ll} \zeta_{\text{TD}} = \dfrac{\sigma_I + P/2}{2\dot{\epsilon}_I} = \dfrac{x_{\text{TD}} + 1/2}{2\dot{\epsilon}_I}P, & \text{(19)} \\[4mm] \eta_{\text{TD}} = \dfrac{\sigma_{II}}{2\dot{\epsilon}_{II}} = \dfrac{y}{2\dot{\epsilon}_{II}}P = \dfrac{-(x_{\text{TD}} - k_t)(1 + x_{\text{TD}})^{\frac{1}{2}}}{2\dot{\epsilon}_{II}}P, & \text{(20)} \end{array} \right\} \text{ for the TD,}$$

and

$$\left.\begin{aligned}
\zeta_{\mathrm{PL}} &= \frac{\sigma_{\mathrm{I}} + P/2}{2\dot{\epsilon}_{\mathrm{I}}} = \frac{x_{\mathrm{PL}} + 1/2}{2\dot{\epsilon}_{\mathrm{I}}}P, \\
\eta_{\mathrm{PL}} &= \frac{\sigma_{\mathrm{II}}}{2\dot{\epsilon}_{\mathrm{II}}} = \frac{y}{2\dot{\epsilon}_{\mathrm{II}}}P = \frac{-(x_{\mathrm{PL}} - k_t)(1 + x_{\mathrm{PL}})}{2\dot{\epsilon}_{\mathrm{II}}}P,
\end{aligned}\right\} \text{ for the PL.}$$
(21)
(22)

In the limit where deformations tend to zero, the viscous coefficients η and ζ become infinite. To avoid this, ζ is capped with a maximum value, $\zeta_{\max}$. In contrast to the elliptical yield curve in the standard VP model, η is not a function of ζ and is also capped at a maximum value $\eta_{\max}$ ($= \zeta_{\max}$, J. Zhang, personal communication).

In Zhang and Rothrock (2005), the following conditions are used for the narrow tip of the TD and PL yield curves:

$$\sigma_{\mathrm{I}} = k_t P \text{ for } l > 1, \text{ for the TD and PL,}$$
(23)

$$\sigma_{\mathrm{I}} = -P \text{ for } l < -1, \text{ for the PL.}$$
(24)

The number l is the link to the orientation of the flow rule, as it is the ratio of divergence and shear. The reasons why stress states with the flow rule oriented such that $|l| \geq 1$ are not allowed is unclear. In addition, the conditions (23, 24) are not required for the mathematical derivation of Eqs. (13) and (16). We discuss this issue in Sect. 3.2.

3 Problems and solutions

The formulation (13), (19), (20) — and (16), (21), (22) — of the constitutive equations, as defined in Zhang and Rothrock (2005), leads to three problems which are addressed in the following sections:

- Section **3.1** – Negative and zero bulk viscosities ζ near the yield curve's apex
- Section **3.2** – Zero shear viscosities η at the yield curves' pointy tips.
- Section **3.3** – Independent viscous capping of ζ and η.

3.1 Negative bulk viscosity

In Eq. (19) and Eq. (21), the bulk viscosity ζ is negative when the numerator and denominator have different signs, i.e., for:

$$-\frac{(2 - k_t)P}{3} < \sigma_{\mathrm{I}} < -\frac{P}{2}, \text{ for the TD,}$$
(25)

$$-\frac{P}{2} < \sigma_{\mathrm{I}} < -\frac{(1 - k_t)P}{2}, \text{ for the PL.}$$
(26)

These regions are marked in red on Fig. 1. In Zhang and Rothrock (2005), the negative ζ are capped at zero ($\zeta_{\min} = 0$, J. Zhang, personal communication). This leads to a void in the yield curve and stress states outside of the yield curve near its apex (see region [1] on Figure 2a). Stress states outside of the yield curve violate the principle of the plastic yield curve: for a given ratio of compressive to shear stress, once the stress magnitude reached the yield criterion, the stresses keep constant while the strain rates can vary.

Negative bulk viscosities appear because the constitutive relation Eq. (2) (or Eq. 4) is derived for a yield curve that is symmetric around $\sigma_{\mathrm{I}} = -\frac{P}{2}$ with zero tensile strength ($k_t = 0$) but does not apply to the non-symmetrical teardrop or symmetrical parabolic lens yield curves with normal flow rules but non-zero tensile strength.

To rewrite the equation, we follow the same method König Beatty and Holland (2010) used for adding tensile strength to the elliptical yield curve. We consider a constitutive equation written as

$$\sigma_{\mathrm{I}} = 2\zeta\dot{\epsilon}_{\mathrm{I}} - p(P, k_t) \tag{27}$$

where p is the constant pressure term we want to find as a function of P and k_t.

Rewriting Eqs. (13) and (16) as a linear function of the divergence $\dot{\epsilon}_{\mathrm{I}}$ and a strain-rate independent part (the pressure term), we obtain,

$$\sigma_{\mathrm{I}} = 2\underbrace{\frac{P}{9\dot{\epsilon}_{\mathrm{II}}}\left(\frac{\dot{\epsilon}_{\mathrm{I}}}{\dot{\epsilon}_{\mathrm{II}}} + \sqrt{\left(\frac{\dot{\epsilon}_{\mathrm{I}}}{\dot{\epsilon}_{\mathrm{II}}}\right)^2 + 3(1 + k_t)}\right)}_{\zeta_{\mathrm{TD}}}\dot{\epsilon}_{\mathrm{I}} - \underbrace{\frac{2 - k_t}{3}P}_{p_{\mathrm{TD}}} \text{ for the TD,} \tag{28}$$

$$\sigma_{\mathrm{I}} = 2\underbrace{\frac{P}{4\dot{\epsilon}_{\mathrm{II}}}}_{\zeta_{\mathrm{PL}}}\dot{\epsilon}_{\mathrm{I}} - \underbrace{\frac{1 - k_t}{2}P}_{p_{\mathrm{PL}}} \text{ for the PL.} \tag{29}$$

By comparing this formulation to Eq (27), new definitions for ζ_{TD} and ζ_{PL} emerge:

$$\zeta_{\mathrm{TD}} = \frac{P}{9\dot{\epsilon}_{\mathrm{II}}}\left(\frac{\dot{\epsilon}_{\mathrm{I}}}{\dot{\epsilon}_{\mathrm{II}}} + \sqrt{\left(\frac{\dot{\epsilon}_{\mathrm{I}}}{\dot{\epsilon}_{\mathrm{II}}}\right)^2 + 3(1 + k_t)}\right) \tag{30}$$

$$\zeta_{\mathrm{PL}} = \frac{P}{4\dot{\epsilon}_{\mathrm{II}}}. \tag{31}$$

and the pressure term becomes $p_{\mathrm{TD}}(P, k_t) = \frac{2 - k_t}{3}P$ and $p_{\mathrm{PL}}(P, k_t) = \frac{1 - k_t}{2}P$. These new formulations for ζ_{TD}, ζ_{PL}, and σ_{I} solve the problem of negative ζ without the need of capping at zero, compared to Eqs. (19) and (21). In this formulation, we let the constitutive equations for σ_{I} and the definition of ζ_{TD} and ζ_{PL} emerge naturally from the system of equations defined by the yield curve and the normal flow rule, without the need to use the constitutive equation of the elliptical yield curve without tensile strength Eq (4).

Note that, for the PL, the pressure term is the same as for the elliptical yield curve with tensile strength (König Beatty & Holland, 2010). The σ_{II} constitutive equation and the shear viscosity η is still computed with Eqs. (5), (20) for the TD, and Eqs. (5), (22) for the PL.

Note that the difference between the pressure term for the original form $\left(\frac{P}{2}\right)$ and the correct form for the TD $\left(\frac{2-k_t}{3}P\right)$ corresponds to the range of σ_{I} where ζ is negative (Eq. 25). The same applies for the PL.

3.2 Zero shear viscosity

The conditions of Eqs. (23, 24) for $l = \frac{\dot{\epsilon}_{\mathrm{I}}}{\dot{\epsilon}_{\mathrm{II}}}$ are not necessary for the derivation of the constitutive equations. In fact, they lead to a discontinuity of the yield curve, where no stress condition is defined, creating a void (region [2] on Fig. 2a). Also, it makes shear viscosities that are equal to zero. This has consequences for the numerical convergence of the momentum equations. Note that for stress states with $|l| > 1$, no LKFs form in the sea ice VP model (see Appendix B, Ringeisen et al., 2019). On the one hand, this may have been the reason that Zhang and Rothrock (2005) introduced the conditions (23, 24). On the other hand, the elliptical yield curve, which serves as our reference for VP sea ice models, allows stress states with $|l| > 1$.

We can replace these conditions by new ones that force the stress states to stay on the pointy tips of the yield curves and avoid $\sigma_{\mathrm{II}} < 0$:

$$\sigma_{\mathrm{I}} = \min(\sigma_{\mathrm{I}}, T), \text{ for the TD and PL} \tag{32}$$

$$\sigma_{\mathrm{I}} = \max(\sigma_{\mathrm{I}}, -P), \text{ for the PL.} \tag{33}$$

However, when σ_{I} is capped like this, the shear viscosity η is identically zero, with $\sigma_{\mathrm{I}} = -P$ and $\sigma_{\mathrm{I}} = k_t P = T$ (Eqs. 20 and 22), and consequently $\sigma_{\mathrm{II}} = 0$. A zero shear viscosity η, while not an energy source as for the negative bulk viscosity, still means less dissipation and may lead to numerical instabilities. Note that even small shear viscosities are sufficient to stabilize the model during large deformations.

The following regularizing conditions on σ_{I} ensure that the TD and PL yield curves are continuous and that $\eta > 0$:

$$\sigma_{\mathrm{I}} = \min(\sigma_{\mathrm{I}}, \alpha T) \text{ for the TD and PL} \tag{34}$$

$$\sigma_{\mathrm{I}} = \max(\sigma_{\mathrm{I}}, -P + \alpha T) \text{ for the PL,} \tag{35}$$

212   where $\alpha \lesssim 1$ (e.g., $\alpha = 0.95$) ensures that η is never equal to zero; i.e., $\sigma_{\mathrm{I}} \neq T$ or $-P$.

213   However, these new conditions truncate the pointy tips of the TD and PL, making them

214   square. With $\alpha \simeq 1$, this truncation is barely noticeable and significantly improves the

215   numerical convergence.

216   ### 3.3   Mixed modes of viscous and plastic deformation

217   When using the teardrop and parabolic lens yield curve with a normal flow rule,

218   viscous creep and plastic deformation are allowed to occur independently from one an-

219   other. For instance, plastic shear deformation is allowed while there is creep in conver-

220   gence. Practically, this means that viscosities ζ and η are capped to ζ_{max} and η_{max} in-

221   dependently, in contrast to the elliptical yield curve where η is a function of ζ and both

222   are capped simultaneously. While this behavior is not physically inconsistent, it leads

223   to stresses outside of the yield curve and stress states inside the yield curve that are plas-

224   tic in one mode or the other. This makes numerical convergence more difficult for a gen-

225   eral yield curve as unequal viscosity can lead to spatial variations of the stress tensor σ,

226   leading to a more complex momentum equation. If the viscosities are equal everywhere,

227   the stress is linear in the deformation and easier to solve.

228   To overcome this issue, we impose limits of ζ and η as

$$\zeta = \min\left(\zeta, \zeta_{\max} \min\left(1, \frac{\zeta}{\eta}\right)\right), \tag{36}$$

$$\eta = \min\left(\eta, \eta_{\max} \min\left(1, \frac{\eta}{\zeta}\right)\right), \tag{37}$$

229   where $\zeta_{\max} = \eta_{\max}$ are model parameters corresponding to ζ_{max} for the elliptical yield

230   curve (Hibler, 1979). With this new relation, we ensure that all stress states inside the

231   yield curve represent viscous deformations and that all stress states on the yield curve

232   represent plastic deformations. This new formulation has the disadvantage that it leads

233   to different maximum viscosity depending on where the viscous stress state is relative

234   to the yield curve. This could be a problem, as stress states inside the yield curve should

235   have a constant viscosity to make the stresses linearly dependent on the strain rates.

236   ### 3.4   Comparison of the original and new formulation

237   Figure 2a shows plastic and stress states with the original and new formulation of

238   the teardrop yield curve. To create these stress states, we create a random field of de-

239   formation rates $\dot{\epsilon}_{ij}$, which contains all combinations of shear, compression, and tension.

240   We then apply the constitutive equation to compute the stresses σ_{ij}. Note that the stress

241   states of both formulations are therefore computed with the same strain rates. The mag-

242   nitude of the random strain rates is set to ensure both viscous and plastic states.
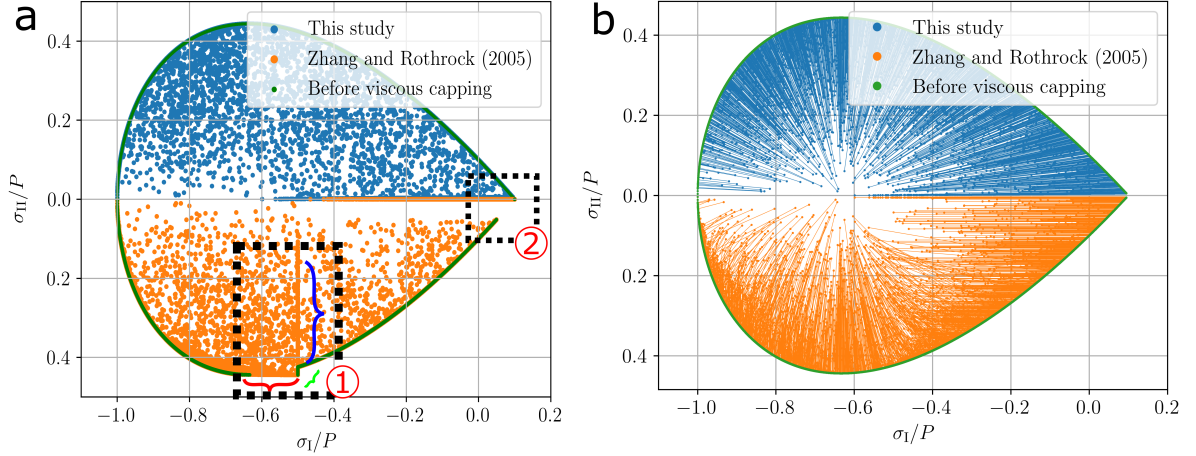
243   With the original simulation, the stress states for which $\zeta = 0$ are outside of the

244   yield curve and gather along the $\sigma_{\mathrm{I}} = \frac{P}{2}$ line — region [1] — and there are no stress

245   states on the yield curve close to the tip — region [2]. These two features do not appear

246   in our modified formulation of the yield curve. The comparison with the PL yield curve

247   shows the same features (not shown).

248   Figure 2b shows the viscous capping process. Before viscous capping, the stresses

249   are all on the yield curve (green). When ζ, or η, are capped independently, the stresses

250   move horizontally, vertically, or towards the center if both viscosities are large enough

251   to be capped (orange lines). When the viscosities are capped together following Eqs. (36–

252   37), the stresses move towards the center of the teardrop (blue lines) $\left(\sigma_{\mathrm{I}} = -\frac{2-k_t}{3}, \sigma_{\mathrm{II}} = 0\right)$.

253   Note that for Fig. 2b, we already use our solutions for η and ζ from Sect. 3.1 and 3.2.

254

4 Experimental setup

256   We use a uniaxial loading experiment in the MIT general circulation model (MITgcm,

257   Campin et al., 2021). A piece of sea ice of $60\,\mathrm{km}$ by $250\,\mathrm{km}$ is embedded in a $100\,\mathrm{km}$ by

258    $260\,\mathrm{km}$ domain with a constant grid spacing of $1\,\mathrm{km}$ (see Fig. 3). The sea ice is $h = 1\,\mathrm{m}$

259   thick and at $A = 100\%$ concentration. The rectangle of ice is in contact with the south-

260   ern border and centered in the domain laterally. Hence, there is $20\,\mathrm{km}$ of open water on

261   the East and West, and $10\,\mathrm{km}$ of open water in the North. We use a no-slip boundary

262   condition for the southern boundary ($u = 0$ and $v \geq 0$). The other boundaries use

263   periodic boundary conditions. Since there is open water to the east, west and north side

264   of the domain, the simulation results are robust with respect to the exact choice of bound-

265   ary conditions on those boundaries. In all simulations below, we use a tensile factor $k_t =$

266   0.05, unless specified otherwise.

267   We use two forcing methods for two different experiments (Circled numbers on Fig. 3):

Figure 2. **(a)** Stress states with the original (orange, lower half plane) and the proposed (blue, upper half plane) formulation of the teardrop yield curve for a random distribution of strain rates. The green lines show the stress rate before the viscous capping. The tensile factor $k_t = 0.1$ and the parameter $\alpha = 0.95$ (see Sect. 3.2). The black boxes [1] and [2] illustrate the issues described in Sect. 3.1 and 3.2. In box [1], the three colors indicate three behaviors: Stress states marked in red exceed the yield curve because of the viscous capping in ζ, and these stresses are displaced horizontally toward the $\frac{P}{2}$ line. In green, some stress states are outside of the yield curve as the bulk viscosity is capped at zero. And in blue, stress states with $\zeta = 0$ move inside the ellipse along the $\frac{P}{2}$ line as η is capped for viscous deformation. **(b)** The lines show the trajectories of the stresses from before viscous capping to after viscous capping in the original (orange, lower half plane) and new formulation (blue, upper half plane) of the viscous capping process (Sect. 3.3). When bulk and shear viscosities are capped independently, the stresses move horizontally or vertically. By capping the viscosities together following Eqs. (36–37), we ensure that the stresses move towards the center of the TD yield curve $\left(\frac{2-k_t}{3}\right)$.
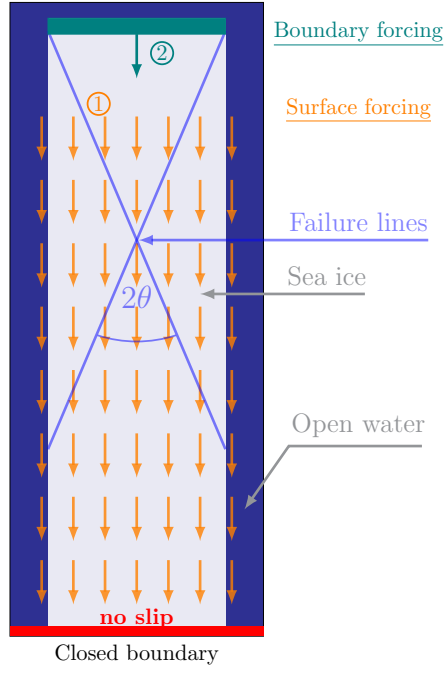
Figure 3. Experimental setup of the idealized experiment. The orange arrows represent the uniform surface stress used for the numerical convergence experiment. The teal area represents the boundary forcing used to investigate the failure angles (Ringeisen et al., 2019). The no-slip closed boundary is shown in red. The blue lines show the failure lines and the failure angle θ, which is half the intersection angle.

1. For the numerical convergence study (Section 5.1), we use a uniform southward surface stress of $0.15\,\mathrm{N\,m}^{-2}$. We use a Picard solver with 10 outer-loop iterations (or pseudo-timesteps) (Zhang & Hibler, 1997), unless otherwise specified. For each of the solver outer-loop iterations, we use an LSR solver to solve the linearized problem until the solution reaches a $10^{-6}\,\mathrm{m\,s}^{-1}$ accuracy or 500 iterations, whichever comes first. These conditions are commonly used for pan-arctic sea ice simulations with 1-2 km resolution (see for example Hutter & Losch, 2020). The timestep is 10 s and the experiment total length is $18\,000\,\mathrm{s}$ or 5 h.

2. For the study of the intersection angles, we prescribe velocity at the border of the sea ice to ensure a uniform stress state in the ice field, as in (Ringeisen et al., 2019). The velocity increases linearly in time, from $v_i = 0\,\mathrm{m\,s}^{-1}$ with a change of $a_v = 5\cdot10^{-4}\,\mathrm{m\,s}^{-2}$. We also use a Picard solver with 1500 outer-loop iterations (or pseudo-timesteps) (Zhang & Hibler, 1997), unless otherwise specified. and we use the LSR solver with a $10^{-11}\,\mathrm{m\,s}^{-1}$ accuracy or 1500 iterations, whichever comes first. The timestep is 0.1 s and the experiment total length is 5 s.

5 Results

5.1 Numerical convergence

Figure 4a shows the L2-norm residual and the number of linear (LSR) iterations for each non-linear loop with the TD yield curve in the idealized experiment described in Sect. 4. The different colors show the residuals with and without the modifications described in Sect. 3, and with the standard elliptical yield curve VP rheology for reference. In the original formulation from Zhang and Rothrock (2005), the model does not converge; i.e., the residual norm increases and stays high. With the new formulation, the model converges and reaches a residual norm similar to the elliptical yield curve with a normal flow rule. The modifications improve the convergence by more than one order of magnitude while decreasing the total number of linear iterations (thus the total simulation time) by nearly two orders of magnitude (Fig.4a).

Figure 4b shows the ten first-time steps of the same experiments but with stricter numerical convergence requirements (the solver's details are listed in the figure caption). Even with a large number of non-linear iterations, the original formulation does not converge and keeps a residual around 10^2. The modified teardrop yield curve can reach a

²⁹⁹ residual of almost 10^{-3} and continues to decrease. However, the rate of decrease is slower than for the elliptical yield curve (Lemieux & Tremblay, 2009).
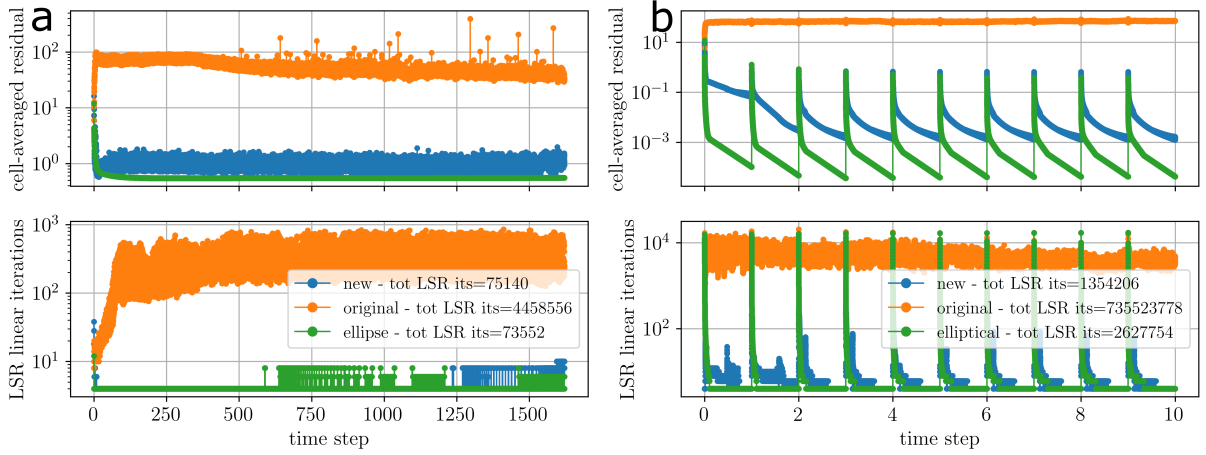
Figure 4. **(a)** L2-norm of the residual and number of linear LSR iterations for each non-linear iteration in each timestep with the teardrop yield curve without (orange) and with (blue) modifications, and with the elliptical yield curve for reference. The number in the legend indicates the total number of linear iterations used in the simulation. We use here commonly used solver settings for a 1 km resolution simulation: 10 outer-loops and 10^{-6} or 500 iterations for the LSR. **(b)** Same as (a), but only the 10 first timesteps when the number of non-linear iterations is increased to 15 000 and the LSR condition for convergence is changed to $10^{-9}\,\mathrm{m\,s^{-1}}$ or 15 000 iterations.

³⁰⁰

³⁰¹ The position of the stress states on or inside the yield curve is an indication of good ³⁰² convergence (Lemieux & Tremblay, 2009). With the new formulation, the stress states ³⁰³ are mostly on or within the yield curve, and the linear structures along $\sigma_\mathrm{I} = -P/2$ and ³⁰⁴ $\sigma_\mathrm{II} = 0$ disappear (Fig. 5).

³⁰⁵ A satisfactory numerical convergence is essential to get the ice dynamic as the rhe-³⁰⁶ ology prescribes (failure angles, ice velocities, etc. . .). We observed that if the residual ³⁰⁷ stays too high, the failure angles do not change according to the rheology (not shown). ³⁰⁸ With only two outer-loops (Zhang & Hibler, 1997; Zhang, 2020), the numerical conver-³⁰⁹ gence of both the original and new formulation is almost the same, and the residual stays ³¹⁰ around $Res \simeq 10^2$, but the number of linear iterations of the new formulation is reduced ³¹¹ (not shown).
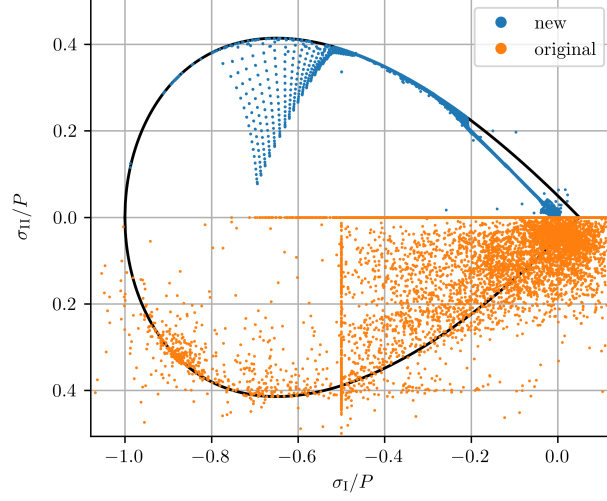
Figure 5. Stress states corresponding to the last timestep of the simulations shown on Fig. 4a. For the new formulation, the stresses form a line following the $\sigma_{\mathrm{II}} = -\sigma_{\mathrm{I}}$ axis, as expected for uniaxial compression (Ringeisen et al., 2019). This line of stress states is grid cells deforming viscously with small stresses gradually increasing southward as the stresses build up.

5.2 Failure angles

5.2.1 Theoretical failure angle

The formulation of the TD and PL yield curve use a normal flow rule, so both the Roscoe theory (Roscoe, 1970) and Coulomb (Coulomb, 1776) predict the same LKFs orientation (Vermeer, 1990). Therefore we use the failure angle prediction as in Ringeisen et al. (2019). We use the normalized stress invariants $\sigma'_{\mathrm{I}} = \frac{\sigma_{\mathrm{I}}}{P}$ and $\sigma'_{\mathrm{II}} = \frac{\sigma_{\mathrm{II}}}{P}$. Because the loading is uni-axial, the stress at failure is given by $\sigma'_{\mathrm{II}} = -\sigma'_{\mathrm{I}}$ (Ringeisen et al., 2019). For the TD yield curve, it means that

$$-\sigma'_{\mathrm{I},s} = -(\sigma'_{\mathrm{I},s} - k_t)\sqrt{1 + \sigma'_{\mathrm{I},s}}; \tag{38}$$

which can be written in the cubic form $x^3 + a_2 x^2 + a_1 x + a_0$

$$\sigma'^{3}_{\mathrm{I},s} - 2k_t\sigma'^{2}_{\mathrm{I},s} + (k_t^2 - 2k_t)\sigma'_{\mathrm{I},s} - k_t^2 = 0. \tag{39}$$

This equation can be solved by using Vieta's substitution (Bronshtein et al., 2015), and we call the only possible solution $\sigma'_{\mathrm{I},s}$. The full derivation of this solution is shown in Appendix A.

The theoretical failure angle is given by

$$\theta_{\mathrm{TD}} = \frac{1}{2} \arccos\left(-\frac{\partial \sigma'_{\mathrm{II}}}{\partial \sigma'_{\mathrm{I}}} (k_t, \sigma'_{\mathrm{I},s}) \right) \tag{40}$$

with the slope of the yield curve teardrop yield curve given by

$$\frac{\partial \sigma'_{\mathrm{II}}}{\partial \sigma'_{\mathrm{I}}} (k_t, \sigma'_{\mathrm{I},s}) = -\frac{2 - k_t + 3\sigma'_{\mathrm{I},s}}{2\sqrt{1 + \sigma'_{\mathrm{I},s}}}. \tag{41}$$

We repeat the same steps for the parabolic lens yield curve, with simpler mathematics as the PL equation is second-order. Eq. (38) becomes

$$-\sigma'^p_{\mathrm{I}} = -(\sigma'^p_{\mathrm{I}} - k_t)(\sigma'^p_{\mathrm{I}} + 1), \tag{42}$$

and its solution

$$\sigma'^p_{\mathrm{I}} = \frac{k_t - \sqrt{k_t^2 + 4k_t}}{2}. \tag{43}$$

We exclude the positive solution, as the intersection point is for a negative σ'_{I}. We then compute the slope of this yield curve

$$\frac{\partial \sigma'_{\mathrm{II}}}{\partial \sigma'_{\mathrm{I}}} (\sigma'_{\mathrm{I}}) = 1 - k_t + 2\sigma'_{\mathrm{I}}, \tag{44}$$

and insert the intersection point

$$\frac{\partial \sigma'_{\mathrm{II}}}{\partial \sigma'_{\mathrm{I}}} (\sigma'^p_{\mathrm{I}}) = 1 - \sqrt{k_t^2 + 4k_t}, \tag{45}$$

so that the failure angle as a function of k_t is given by

$$\theta_{\mathrm{PL}}(k_t) = \frac{1}{2} \arccos\left(1 - \sqrt{k_t^2 + 4k_t} \right). \tag{46}$$

5.2.2 Modeled failure angles

We investigate the dependence of the failure angles on the tensile factor k_t, which is the only parameter in the TD and PL rheologies besides $P^\star$. The failure lines, or LKFs, form a diamond for both rheologies, as observed with other yield curves (Ringeisen et al., 2019). We measure the angle of failure θ, which corresponds to half of the intersection between the LKF, as shown on Fig. 3.

For $k_t < 0.05$, the failure angles are below $30°$, the minimum value that can be reached for the elliptical yield curve with a normal flow rule. The angle of failure increases with k_t, in agreement with the theoretical predictions (Figure 6). The modeled angles of failure agree with the theoretical predictions: For the TD rheology, the RMS error and

the R^2 number between the modeled angles and the predictions are $0.458°$ and 0.992.

For the PL rheology, the RMS error is $0.24°$, and the R^2 is 0.998. Such an agreement

was expected as the TD and PL yield curves use a normal flow rule, as the elliptical yield

curve (Ringeisen et al., 2019). Note that for the same value of k_t, the failure angles of

the parabolic lens rheology are always larger than with the teardrop rheology.
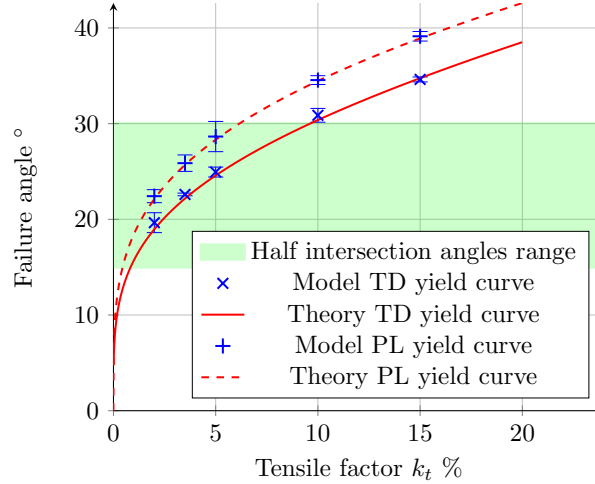
Figure 6. Failure angles (The half of the LKFs intersection angles) for the Teardrop (TD) and the Parabolic Lens (PL) yield curve. The error ranges correspond to 2σ deviations. The shaded green area on the graph shows the range of the peak of failure angles in RGPS observations (Hutter et al., 2022). The angles from the theory are given by Eq. (40) for the TD and Eq. (46) for the PL.

6 Discussion

The problems in the TD and PL formulation seem to have gone unnoticed because of the generally small number of solver outer-loops used in sea ice models. Sea ice models that use these yield curves generally use a very limited number of non-linear iterations (2 pseudo-timesteps, Zhang & Hibler, 1997). In this case, issues in the model's formulation remain hidden behind the unconverged solution. By investigating the formulations of sea ice models in idealized simulations where numerical convergence can be attempted, problems can be identified, investigated, and solved.

340   The reasons for the slower convergence with the TD are unclear but may be caused

341 by varying viscosity inside the yield curve. For the elliptical yield curve with $P = \text{const}$,

342 the stress states within the yield curve always have the same viscosities ($\zeta = \zeta_{\max}$ and

343 $\eta = \frac{\zeta_{\max}}{e^2}$). With the TD and PL yield curves, the viscosities are defined independently

344 and the transition from plastic to viscous deformations also has to be treated indepen-

345 dently (see Sect. 3.3). For small stresses (i.e., σ_{I} and $\sigma_{\mathrm{II}} \simeq 0$), this leads to unphysi-

346 cal gradients of shear viscosity. These gradients lead to spatial stress variations, thus small-

347 scale viscous deformations. These variations in deformations make the numerical con-

348 vergence more difficult for the TD compared to the elliptical yield curve. This behav-

349 ior leads to the cloud of points close to $\sigma_{\mathrm{I}} = 0$ on Fig. 5.

350   Both rheologies show good agreement with the theoretical prediction of failure an-

351 gles with a normal flow rule. The TD and PL rheologies have two advantages: (1) They

352 create angles smaller than the elliptical yield curve (Ringeisen et al., 2019)and in the range

353 of observations (Hutter et al., 2022; Erlingsson, 1988) when used with a small tensile strength

354 factor ($k_t < 5\%$); and (2) they feature a normal flow rule, which is better to solve nu-

355 merically compared to the elliptical yield curve with non-normal flow rule (Ringeisen et

356 al., 2021). About the relevance of the TD and PL yield curves, we see two drawbacks:

357 (1) The shape of the yield curve only has one parameter, k_t, while the elliptical yield curve

358 has e and k_t. (2) More surface of the TD yield curve is dedicated to a divergent flow rule,

359 while the elliptical yield curve and the PL yield curve have the same surface dedicated

360 to convergent and divergent deformations. The effect of the difference of divergence and

361 convergence surface on the yield curve will need to be investigated in a pan-arctic setup.

7 Summary and Conclusions

363   A new formulation of the teardrop (TD) and parabolic lens (PL) yield curves with

364 normal flow rule addresses three problems in its original formulation (Zhang & Rothrock,

365 2005). Two of these problems have a common cause: zero bulk or shear viscosity. The

366 zero bulk viscosity ζ is a consequence of the assumption that the constitutive equation

367 Eq. (2) presented in Hibler (1979) is valid for all yield curves, including asymmetrical

368 ones with respect to an average internal pressure $\frac{P}{2}$ and with non-zero tensile strength.

369 When letting the constitutive equation emerge naturally from the yield curve equation

370 and the normal flow rule conditions, a similar relation is found, except for the pressure

371 term with a new scaling factor different from $\frac{1}{2}$ that is a function of k_t. With this mod-

372 ification, negative bulk viscosities in the original formulation no longer appear, and ad-

373 ditional limiting from below is unnecessary. The zero shear viscosity η is a consequence

374 of the condition that keeps stress at the pointy tips (at $\sigma_I = T$ or $-P$) of the yield curves.

375 These conditions of the original formulation are independent of k_t, leading to a discon-

376 tinuity on the yield curve. The identically zero shear viscosity leads to instabilities. This

377 problem can be fixed by cutting the tip before it reaches the σ_I axis, ensuring a contin-

378 uous yield curve and non-zero viscosities.

379 The third problem, of lesser importance, is linked to the capping of the viscosities

380 for the transition from plastic to viscous states. We reformulate the maximum limit on

381 the bulk and shear viscosities to ensure that both are capped consistently and not in-

382 dependently. By doing so, we avoid stress states that represent half-viscous and half-plastic

383 deformation. The direct consequence of these changes is an improved numerical conver-

384 gence and stress states that are on or within the yield curve. The most important was

385 to avoid negative and zero viscosities.

386 We show that for small values of the tensile strength factors, i.e., $k_t < 0.05$, the

387 TD and PL yield curves can create smaller angles than the elliptical yield curve in uni-

388 axial compression. The shape of the TD yield curve resembles the shape of the Mohr–

389 Coulomb yield curve and eliminates non-differentiable points when compared with other

390 yield curves like the curved diamond yield curve (Wang, 2007) or the Coulombic yield

391 curves (Hibler & Schulson, 2000). This makes the teardrop yield curve an interesting al-

392 ternative for general use in the community.

393 **Appendix A Solving for the angle for the TD yield curve**

We solve the cubic equation that determines the coordinates of the intersection point between the teardrop yield curve and the $\sigma_{II} = -\sigma_I$ axis. This equation of the cubic form $x^3 + a_2 x^2 + a_1 x + a_0$ is written

$$\sigma_{I,s}^{'3} - 2k_t \sigma_{I,s}^{'2} + (k_t^2 - 2k_t)\sigma_{I,s}' - k_t^2 = 0. \tag{A1}$$

We solve this equation using Vieta's substitution (Bronshtein et al., 2015): we define Q and R

$$Q = \frac{3a_1 - a_2^2}{9} = \frac{-6k_t - k_t^2}{9} \tag{A2}$$

$$R = \frac{9a_1 a_2 - 27a_0 - 2a_2^3}{54} = \frac{18k_t^3 - 36k_t^2 - 27k_t^2 - 16k_t^3}{54} \tag{A3}$$

from which we compute the determinant

$$D = Q^3 + R^2 \tag{A4}$$

If $D < 0$, then three distinct real solutions exist. Note that, because we compute the intersection of two curves (the axis $\sigma_{II} = -\sigma_I$, and the yield curve), the solutions are real and not complex. The three real solutions are defined by

$$x_1 = 2\sqrt{-Q} \cos\left(\frac{\theta}{3}\right) - \frac{1}{3}a_2 \tag{A5}$$

$$x_2 = 2\sqrt{-Q} \cos\left(\frac{\theta + 2\pi}{3}\right) - \frac{1}{3}a_2 \tag{A6}$$

$$x_3 = 2\sqrt{-Q} \cos\left(\frac{\theta + 4\pi}{3}\right) - \frac{1}{3}a_2 \tag{A7}$$

where

$$\theta = \cos^{-1}\left(\frac{R}{\sqrt{-Q^3}}\right) \tag{A8}$$

Among these three solutions, x_1 and x_3 are positive, and x_2 is negative (not shown). We search for a negative solution because we only consider a compressive state (i.e., $\sigma_I < 0$), so $\sigma'_{I,s} = x_2$ is the correct intersection solution.

For details, the first solution x_1 is the intersection of the yield curve and the axis defined by $\sigma_{II} = -\sigma_I$ for $\sigma_I > k_t$, while the third solution x_3 is the intersection point of the yield curve symmetrical compared to the axis σ_I and comes from the square power used between Eqs. (38) and (39), $x_3 \in [0, k_t]$.

Open Research - Availability Statement

Acknowledgments

References

⁴¹⁹ Bouchat, A., Hutter, N., Chanut, J., Dupont, F., Dukhovskoy, D., Garric, G., . . .

⁴²⁰   Wang, Q. (2022). Sea Ice Rheology Experiment (SIREx): 1. Scaling and

⁴²¹   Statistical Properties of Sea-Ice Deformation Fields. *Journal of Geophysi-*

⁴²²   *cal Research: Oceans*, *127*(4), e2021JC017667. Retrieved 2022-08-16, from

⁴²³   `https://onlinelibrary.wiley.com/doi/abs/10.1029/2021JC017667`

⁴²⁴   (_eprint: https://onlinelibrary.wiley.com/doi/pdf/10.1029/2021JC017667)

⁴²⁵   doi: 10.1029/2021JC017667

⁴²⁶ Bouchat, A., & Tremblay, B. (2017). Using sea-ice deformation fields to con-

⁴²⁷   strain the mechanical strength parameters of geophysical sea ice. *Jour-*

⁴²⁸   *nal of Geophysical Research: Oceans*, n/a–n/a. Retrieved 2017-06-20, from

⁴²⁹   `http://onlinelibrary.wiley.com/doi/10.1002/2017JC013020/abstract`

⁴³⁰   doi: 10.1002/2017JC013020

⁴³¹ Bratchie, I. (1984). Rheology of an Ice-Floe Field. *Annals of Glaciology*, *5*, 23–28.

⁴³²   Retrieved 2019-11-04, from `https://www.cambridge.org/core/journals/`

⁴³³   `annals-of-glaciology/article/rheology-of-an-icefloe-field/`

⁴³⁴   `D3D1634B0EFC0C8C53E68B2761C0F773` doi: 10.3189/1984AoG5-1-23-28

⁴³⁵ Bronshtein, I. N., Semendyayev, K. A., Musiol, G., & Mühlig, H. (2015). *Handbook*

⁴³⁶   *of Mathematics* (6th ed. 2015 edition ed.). Heidelberg New York Dordrecht

⁴³⁷   London: Springer.

⁴³⁸ Campin, J.-M., Heimbach, P., Losch, M., Forget, G., Edhill3, Adcroft, A., . . .

⁴³⁹   Dussin, R. (2021, June). *MITgcm/MITgcm: checkpoint67z.* Zenodo.

⁴⁴⁰   Retrieved 2021-07-28, from `https://zenodo.org/record/4968496` doi:

⁴⁴¹   10.5281/ZENODO.4968496

⁴⁴² Coon, M. D., Maykut, G., A., Pritchard, R. S., Rothrock, D. A., & Thorndike, A. S.

⁴⁴³   (1974, May). Modeling The Pack Ice as an Elastic-Plastic Material. *AIDJEX*

444   *BULLETIN*, *No. 24* (Numerical Modeling Report), 1–106.

445 Coulomb, C. A.   (1776).   *Essai sur une application des règles de maximis & min-*

446   *imis à quelques problèmes de statique, relatifs à l'architecture.*   Paris: De

447   l'Imprimerie Royale.

448 Dansereau, V., Weiss, J., Saramito, P., & Lattes, P.   (2016, July).   A Maxwell elasto-

449   brittle rheology for sea ice modelling.   *The Cryosphere*, *10*(3), 1339–1359.

450   Retrieved 2016-10-07, from `http://www.the-cryosphere.net/10/1339/2016/`

451   doi: 10.5194/tc-10-1339-2016

452 Drucker, D. C.   (1950).   Some implications of work hardening and ideal plasticity.

453   *Quarterly of Applied Mathematics*, *7*(4), 411–418.

454 Dukowicz, J. K.   (1997, March).   Comments on "Stability of the Viscous–Plastic Sea

455   Ice Rheology".   *Journal of Physical Oceanography*, *27*(3), 480–481.   Retrieved

456   2021-11-16, from `https://journals.ametsoc.org/view/journals/phoc/`

457   `27/3/1520-0485_1997_027_0480_cosotv_2.0.co_2.xml`   (Publisher: Ameri-

458   can Meteorological Society Section: Journal of Physical Oceanography)   doi:

459   10.1175/1520-0485(1997)027⟨0480:COSOTV⟩2.0.CO;2

460 Erlingsson, B.   (1988).   Two-dimensional deformation patterns in sea ice.   *Journal of*

461   *Glaciology*, *34*(118), 301–308.

462 Girard, L., Weiss, J., Molines, J. M., Barnier, B., & Bouillon, S.   (2009, August).

463   Evaluation of high-resolution sea ice models on the basis of statistical and

464   scaling properties of Arctic sea ice drift and deformation.   *Journal of Geo-*

465   *physical Research: Oceans*, *114*(C8), C08015.   Retrieved 2016-11-14, from

466   `http://onlinelibrary.wiley.com/doi/10.1029/2008JC005182/abstract`

467   doi: 10.1029/2008JC005182

468 Hibler, W. D.   (1977, September).   A viscous sea ice law as a stochastic average of

469   plasticity.   *Journal of Geophysical Research*, *82*(27), 3932–3938.   Retrieved

470   from `http://onlinelibrary.wiley.com/doi/10.1029/JC082i027p03932/`

471   `abstract`   doi: 10.1029/JC082i027p03932

472 Hibler, W. D.   (1979, July).   A Dynamic Thermodynamic Sea Ice Model.   *Jour-*

473   *nal of Physical Oceanography*, *9*(4), 815–846.   Retrieved 2016-10-07, from

474   `http://journals.ametsoc.org/doi/abs/10.1175/1520-0485%281979%`

475   `29009%3C0815%3AADTSIM%3E2.0.CO%3B2`   doi: 10.1175/1520-0485(1979)

476   009⟨0815:ADTSIM⟩2.0.CO;2

Hibler, W. D., & Schulson, E. M. (2000, July). On modeling the anisotropic failure and flow of flawed sea ice. *Journal of Geophysical Research: Oceans*, *105*(C7), 17105–17120. Retrieved 2017-02-02, from `http://onlinelibrary.wiley.com/doi/10.1029/2000JC900045/abstract` doi: 10.1029/2000JC900045

Hutchings, J. K., Heil, P., & Hibler, W. D. (2005, December). Modeling Linear Kinematic Features in Sea Ice. *Monthly Weather Review*, *133*(12), 3481–3497. Retrieved 2017-02-09, from `http://journals.ametsoc.org/doi/abs/10.1175/MWR3045.1` doi: 10.1175/MWR3045.1

Hutter, N., Bouchat, A., Dupont, F., Dukhovskoy, D., Koldunov, N., Lee, Y. J., ... Wang, Q. (2022). Sea Ice Rheology Experiment (SIREx): 2. Evaluating Linear Kinematic Features in High-Resolution Sea Ice Simulations. *Journal of Geophysical Research: Oceans*, *127*(4), e2021JC017666. Retrieved 2022-08-16, from `https://onlinelibrary.wiley.com/doi/abs/10.1029/2021JC017666` (_eprint: https://onlinelibrary.wiley.com/doi/pdf/10.1029/2021JC017666) doi: 10.1029/2021JC017666

Hutter, N., & Losch, M. (2020, January). Feature-based comparison of sea ice deformation in lead-permitting sea ice simulations. *The Cryosphere*, *14*(1), 93–113. Retrieved 2020-02-24, from `https://www.the-cryosphere.net/14/93/2020/` doi: 10.5194/tc-14-93-2020

Hutter, N., Zampieri, L., & Losch, M. (2019, February). Leads and ridges in Arctic sea ice from RGPS data and a new tracking algorithm. *The Cryosphere*, *13*(2), 627–645. Retrieved 2020-03-21, from `https://www.the-cryosphere.net/13/627/2019/` (Publisher: Copernicus GmbH) doi: https://doi.org/10.5194/tc-13-627-2019

Iliescu, D., & Schulson, E. M. (2004, December). The brittle compressive failure of fresh-water columnar ice loaded biaxially. *Acta Materialia*, *52*(20), 5723–5735. Retrieved 2022-11-24, from `https://www.sciencedirect.com/science/article/pii/S1359645404004355` doi: 10.1016/j.actamat.2004.07.027

Ip, C. F., Hibler, W. D., & Flato, G. M. (1991). On the effect of rheology on seasonal sea-ice simulations. *Annals of Glaciology*, *15*, 17–25.

Koldunov, N. V., Danilov, S., Sidorenko, D., Hutter, N., Losch, M., Goessling, H., ... Jung, T. (2019). Fast EVP Solutions in a High-Resolution Sea Ice Model. *Journal of Advances in Modeling Earth Systems*, *11*(5), 1269–1284. Retrieved

2020-02-10, from `https://agupubs.onlinelibrary.wiley.com/doi/abs/`
`10.1029/2018MS001485` doi: 10.1029/2018MS001485

Kwok, R.   (2001).   Deformation of the Arctic Ocean Sea Ice Cover between
November 1996 and April 1997: A Qualitative Survey.   In J. P. Dempsey &
H. H. Shen (Eds.), *IUTAM Symposium on Scaling Laws in Ice Mechanics*
and Ice Dynamics (pp. 315–322).   Dordrecht: Springer Netherlands.   doi:
10.1007/978-94-015-9735-7

König Beatty, C., & Holland, D. M.   (2010, January).   Modeling Landfast Sea Ice
by Adding Tensile Strength.   *Journal of Physical Oceanography*, *40*(1), 185–
198.   Retrieved 2017-05-15, from `http://journals.ametsoc.org/doi/abs/`
`10.1175/2009JPO4105.1` doi: 10.1175/2009JPO4105.1

Lemieux, J.-F., & Tremblay, B.   (2009, May).   Numerical convergence of viscous-
plastic sea ice models.   *Journal of Geophysical Research: Oceans*, *114*(C5).
Retrieved 2018-11-05, from `https://agupubs.onlinelibrary.wiley.com/`
`doi/abs/10.1029/2008JC005017` doi: 10.1029/2008JC005017

Losch, M., & Danilov, S.   (2012).   On solving the momentum equations of dynamic
sea ice models with implicit solvers and the elastic–viscous–plastic technique.
Ocean Modelling, *41*, 42–52.

Losch, M., Menemenlis, D., Campin, J.-M., Heimbach, P., & Hill, C. (2010). On the
formulation of sea-ice models. Part 1: Effects of different solver implementa-
tions and parameterizations.   *Ocean Modelling*, *33*(1–2), 129–144.   Retrieved
2017-01-31, from `https://www.sciencedirect.com/science/article/pii/`
`S1463500309002418` doi: 10.1016/j.ocemod.2009.12.008

Marshall, J., Adcroft, A., Hill, C., Perelman, L., & Heisey, C.   (1997, March).   A
finite-volume, incompressible Navier Stokes model for studies of the ocean on
parallel computers.   *Journal of Geophysical Research: Oceans*, *102*(C3), 5753–
5766.   Retrieved 2017-02-27, from `http://onlinelibrary.wiley.com/doi/`
`10.1029/96JC02775/abstract` doi: 10.1029/96JC02775

Maykut, G. A.   (1978).   Energy exchange over young sea ice in the cen-
tral Arctic.   *Journal of Geophysical Research: Oceans*, *83*(C7), 3646–
3658.   Retrieved 2020-06-02, from `https://agupubs.onlinelibrary`
`.wiley.com/doi/abs/10.1029/JC083iC07p03646`   (_eprint:
https://agupubs.onlinelibrary.wiley.com/doi/pdf/10.1029/JC083iC07p03646)

doi: 10.1029/JC083iC07p03646

Notz, D., & Community, S. (2020). Arctic Sea Ice in CMIP6. *Geophysical Research Letters*, *47*(10), e2019GL086749. Retrieved 2021-11-24, from `https://onlinelibrary.wiley.com/doi/abs/10.1029/2019GL086749` (_eprint: https://onlinelibrary.wiley.com/doi/pdf/10.1029/2019GL086749) doi: 10.1029/2019GL086749

Palmer, A. C., Maier, G., & Drucker, D. C. (1967). Normality relations and convexity of yield surfaces for unstable materials or structural elements.

Pritchard, R. S. (2005). Stability of sea ice dynamics models: Viscous-plastic rheology, replacement closure, and tensile cutoff. *Journal of Geophysical Research: Oceans*, *110*(C12). Retrieved 2020-10-29, from `https://agupubs.onlinelibrary.wiley.com/doi/abs/10.1029/2003JC001875` (_eprint: https://agupubs.onlinelibrary.wiley.com/doi/pdf/10.1029/2003JC001875) doi: 10.1029/2003JC001875

Richter-Menge, J. A., & Jones, K. F. (1993). The tensile strength of first-year sea ice. *Journal of Glaciology*, *39*(133), 609–618. Retrieved 2019-03-19, from `https://www.cambridge.org/core/journals/journal-of-glaciology/article/tensile-strength-of-firstyear-sea-ice/3D163667916EFABC21415F7AF81496FB` doi: 10.3189/S0022143000016506

Ringeisen, D., Losch, M., & Tremblay, B. (2022, February). *MITgcm configuration and simulations for the test of the teardrop yield curve.* Zenodo. Retrieved 2022-02-15, from `https://zenodo.org/record/6091690` (Language: eng) doi: 10.5281/zenodo.6091690

Ringeisen, D., Losch, M., Tremblay, L. B., & Hutter, N. (2019, April). Simulating intersection angles between conjugate faults in sea ice with different viscous–plastic rheologies. *The Cryosphere*, *13*(4), 1167–1186. Retrieved 2019-05-08, from `https://www.the-cryosphere.net/13/1167/2019/` doi: https://doi.org/10.5194/tc-13-1167-2019

Ringeisen, D., Tremblay, L. B., & Losch, M. (2021, June). Non-normal flow rules affect fracture angles in sea ice viscous–plastic rheologies. *The Cryosphere*, *15*(6), 2873–2888. Retrieved 2021-06-29, from `https://tc.copernicus.org/articles/15/2873/2021/` (Publisher: Copernicus GmbH) doi: 10.5194/tc-15-2873-2021

576 Roscoe, K. H.   (1970, June).   The Influence of Strains in Soil Mechanics.
577   *Géotechnique*, *20*(2), 129–170.   Retrieved 2020-02-20, from `https://`
578   `www.icevirtuallibrary.com/doi/abs/10.1680/geot.1970.20.2.129`   doi:
579   10.1680/geot.1970.20.2.129

580 Rothrock, D. A.   (1975, November).   The energetics of the plastic deformation of
581   pack ice by ridging.   *Journal of Geophysical Research*, *80*(33), 4514–4519.   Re-
582   trieved 2016-10-10, from `http://onlinelibrary.wiley.com/doi/10.1029/`
583   `JC080i033p04514/abstract` doi: 10.1029/JC080i033p04514

584 Schulkes, R. M. S. M. (1996, February). Asymptotic Stability of the Viscous–Plastic
585   Sea Ice Rheology.   *Journal of Physical Oceanography*, *26*(2), 279–283.   Re-
586   trieved 2021-11-16, from `https://journals.ametsoc.org/view/journals/`
587   `phoc/26/2/1520-0485_1996_026_0279_asotvs_2_0_co_2.xml`   (Publisher:
588   American Meteorological Society Section: Journal of Physical Oceanography)
589   doi: 10.1175/1520-0485(1996)026⟨0279:ASOTVS⟩2.0.CO;2

590 Schulson, E. M.   (2004, July).   Compressive shear faults within arctic sea ice: Frac-
591   ture on scales large and small.   *Journal of Geophysical Research: Oceans*,
592   *109*(C7), C07016.   Retrieved 2017-12-18, from `http://onlinelibrary.wiley`
593   `.com/doi/10.1029/2003JC002108/abstract` doi: 10.1029/2003JC002108

594 Tremblay, L.-B., & Mysak, L. A. (1997, November). Modeling Sea Ice as a Granular
595   Material, Including the Dilatancy Effect.   *Journal of Physical Oceanography*,
596   *27*(11), 2342–2360.   Retrieved 2017-02-24, from `http://journals.ametsoc`
597   `.org/doi/abs/10.1175/1520-0485(1997)027%3C2342:MSIAAG%3E2.0.CO;2`
598   doi: 10.1175/1520-0485(1997)027⟨2342:MSIAAG⟩2.0.CO;2

599 Tsamados, M., Feltham, D. L., & Wilchinsky, A. V.   (2013, January).   Impact
600   of a new anisotropic rheology on simulations of Arctic sea ice.   *Journal of*
601   *Geophysical Research: Oceans*, *118*(1), 91–107.   Retrieved 2016-11-08, from
602   `http://onlinelibrary.wiley.com/doi/10.1029/2012JC007990/abstract`
603   doi: 10.1029/2012JC007990

604 Vermeer, P. A.   (1990).   The orientation of shear bands in biaxial tests.
605   *Géotechnique*.   Retrieved 2019-08-26, from `https://www.icevirtuallibrary`
606   `.com/doi/abs/10.1680/geot.1990.40.2.223`   doi: 10.1680/geot.1990.40.2
607   .223

608 Wang, K. (2007, May). Observing the yield curve of compacted pack ice. *Journal of*

609   *Geophysical Research: Oceans*, *112*(C5), C05015.   Retrieved 2017-12-12, from

610   `http://onlinelibrary.wiley.com/doi/10.1029/2006JC003610/abstract`

611   doi: 10.1029/2006JC003610

612   Zhang, J.   (2020).   Sea ice properties in high-resolution sea ice

613   models.   *Journal of Geophysical Research: Oceans*, *n/a*(n/a),

614   e2020JC016689.   Retrieved 2020-12-14, from `https://agupubs`

615   `.onlinelibrary.wiley.com/doi/abs/10.1029/2020JC016686`   (_eprint:

616   https://agupubs.onlinelibrary.wiley.com/doi/pdf/10.1029/2020JC016686)   doi:

617   https://doi.org/10.1029/2020JC016686

618   Zhang, J., & Hibler, W. D.   (1997, April).   On an efficient numerical method for

619   modeling sea ice dynamics. *Journal of Geophysical Research: Oceans*, *102*(C4),

620   8691–8702.   Retrieved 2016-11-23, from `http://onlinelibrary.wiley.com/`

621   `doi/10.1029/96JC03744/abstract` doi: 10.1029/96JC03744

622   Zhang, J., & Rothrock, D. A. (2005, August). Effect of sea ice rheology in numerical

623   investigations of climate.   *Journal of Geophysical Research: Oceans*, *110*(C8),

624   C08014. Retrieved 2017-12-18, from `http://onlinelibrary.wiley.com/doi/`

625   `10.1029/2004JC002599/abstract` doi: 10.1029/2004JC002599